

Estimated relations at a shock driven by a coronal mass ejection

M. Eselevich¹ · V. Eselevich¹

© Springer ●●●●

Abstract Analysis of SOHO/LASCO C3 data reveals a discontinuity, interpreted as a shock wave, in plasma density radial profiles in a restricted region ahead of each of ten selected coronal mass ejections (CME) along their travel directions. In various events, shock wave velocity $V \approx 800\text{--}2500 \text{ km s}^{-1}$. Comparing the dependence of Alfvén Mach number M_A on shock wave strength ρ_2/ρ_1 , measured at $R > 10R_\odot$ from the center of the Sun, to ideal MHD calculations suggests that the effective adiabatic index γ , characterizing the processes inside the shock front, is largely between 2 and $5/3$. This corresponds to the effective number of degrees of freedom of motion 2 to 3. A similar dependence, $M_A(\rho_2/\rho_1)$, was derived for the Earth’s bow shock and interplanetary collisionless shock waves. All this supports the assumption that the discontinuities in front of CMEs are collisionless shock waves.

Keywords: Coronal Mass Ejections, Initiation and Propagation; Waves, Shock

1. Introduction

If the Rankine-Hugoniot relations are valid at the discontinuity in supersonic plasma (or gas) stream parameters, the discontinuity may be interpreted as a shock wave. Even to roughly estimate the validity of these relations for a shock discontinuity driven in front of fast CMEs is no easy task. This is first of all associated with the fact that a shock front is difficult to identify and register in the coronal conditions. Nevertheless, several such attempts for individual events have been made in Vourlidas *et al.*, 2003; Eselevich and Eselevich, 2007; Manchester IV *et al.*, 2008; Eselevich and Eselevich, 2008; Ontiveros and Vourlidas, 2009 (hereafter Paper 1).

Two different approaches may be singled out which have been applied to identifying a shock front on coronal images. The first one is numerical simulation within the framework of the ideal magnetohydrodynamics (MHD) of the entire process of CME formation and propagation. In this case, the manner in which the CME is formed may be arbitrary. The results of such a simulation were compared to the experiment in order to identify the shock front (Vourlidas *et al.*, 2003;

¹ Institute of solar-terrestrial physics, Irkutsk, Russia
email: mesel@iszf.irk.ru email: esel@iszf.irk.ru

Manchester IV *et al.*, 2008). Note that in this case one can directly estimate the relation between thermodynamic parameters at the discontinuity because they are included in the model.

The second approach relies on the fact that there is no shock discontinuity if the velocity of the generating CME remains below the critical velocity, u_C ; while such a discontinuity does exist at supercritical velocities. Regardless of the difficulty in estimating the critical velocity in the corona, this approach enabled us to demonstrate that the transition does exist, and consequently the observed discontinuity is a shock wave (Eselevich and Eselevich, 2008). There is some difficulty in identifying the shock fronts in coronal images stemming from the fact that the CME frontal structure and the shock front in front of it are identical geometrically and are often rather close to each other. We employed two different complementary methods to make sure that the observed discontinuity in the brightness distribution is the shock front rather than the CME frontal structure behind it:

1. We examined the conditions in the disturbed zone in front of CMEs with different velocities u . For CMEs with velocities exceeding u , the shock-wave-related discontinuity was observed in the frontal part of a rather extended disturbed zone.
2. The processes of the disturbed zone evolution and shock wave formation were investigated for some CMEs, in the coordinate system associated with their frontal structures, when the CME velocity u passes the critical velocity u_C (Eselevich, 2010).

Note that the value of the critical velocity at which a shock wave formed appeared to be rather close to existing estimates of the Alfvén velocity in the corona (Mann *et al.*, 1999). These methods allowed the shock front width to be measured for several tens of CMEs at various distances (up to $6R_\odot$) from the center of the Sun (R_\odot is the Sun’s radius).

Thus, whether by one or another method, we can identify a shock wave in the corona; so the next obvious step would be to try to verify the validity of the Rankine-Hugoniot relations at the shock. We are restricted, however, in that we cannot measure just *any* plasma parameter in the corona. White-light coronal images allow the shock discontinuity velocity to be determined (from the change in the discontinuity position with time) and the density ratio estimated at the discontinuity, relying on some assumptions. Apparently, it is these values that should be taken as a basis for the analysis. Moreover, similarly to the Earth’s bow shock, we may apply simple relations of the ideal MHD at a flat shock discontinuity to investigate shocks in the corona, i.e. make use of the assumption that the shock front width is smaller than the radius of its curvature.

The aim of this work is to obtain Rankine-Hugoniot relations at the flat shock discontinuity, within the framework of the ideal MHD, and to estimate their validity for a number of identified shocks driven ahead of CMEs.

2. Data and method of analysis

The analysis involved LASCO C3 coronal images with a 4 to 30 R_{\odot} field of view (Brueckner *et al.*, 1995). The images contain many stars that are much brighter than the corona. Such point objects as stars can be easily removed by a sigma filter. The filter is applied to calculating the mean value and rms deviation in a square neighborhood centered at each image pixel, excluding the pixel itself. If the brightness of the central pixel exceeds the mean value by more than a certain value, it is replaced by the mean. The filtering of all images involved a 15×15 pixel neighborhood and a maximum deviation equaling three rms deviations, while the filtering procedure was iterated ten times. After filtration, the images of bright stars are effectively eliminated, the coronal brightness signal remaining almost unchanged.

The images thus processed were presented as difference brightness $\Delta P = P(t) - P(t_0)$, where $P(t)$ is the coronal brightness at instant t , corresponding to the event in question, $P(t_0)$ is the undisturbed brightness at fixed instant t_0 chosen well before the event. Thus, the background brightness due to the stationary distribution of plasma in the corona was eliminated. Calibrated LASCO images with full brightness $P(t)$ (in units of mean solar brightness, P_{MSB}) enable us to use the difference brightness to estimate the mean density of the matter causing the change in brightness, if we make an assumption with regard to its spatial size along the line of sight.

The difference brightness was used to examine the dynamics of CMEs, as well as of the disturbed zone and shock wave in front of them. It has proved to be more convenient to employ maps of difference brightness isolines rather than the traditional grey-scale images for selecting and generally analyzing events. The arrangement of isolines provides for a better understanding of the character of the difference brightness distribution, direction and value of the gradients. Isolines levels were selected depending on the event and the distance at which it was considered.

It is more convenient to make quantitative measurements using difference brightness profiles drawn in a certain direction. For this purpose, we used radial profiles $\Delta P(R)$ of difference brightness drawn from the center of the Sun along the direction of the fixed position angle PA as well as nonradial profiles $\Delta P(r)$ constructed from a specified point and in a specified direction. The notations differ in distance R , plotted from the center of the Sun, and in distance r , plotted from another point on the image. All the distances in the plots and figures are in units of one solar radius (R_{\odot}). In some cases, difference brightness profiles correspond to the finite angle average. The averaging had a purpose of improving the desired signal-to-noise ratio.

3. Relations at a flat shock discontinuity in the ideal MHD approximation

Relations at a discontinuity link various plasma parameters on either side of the shock discontinuity. They enable us to relate the Mach number in the medium

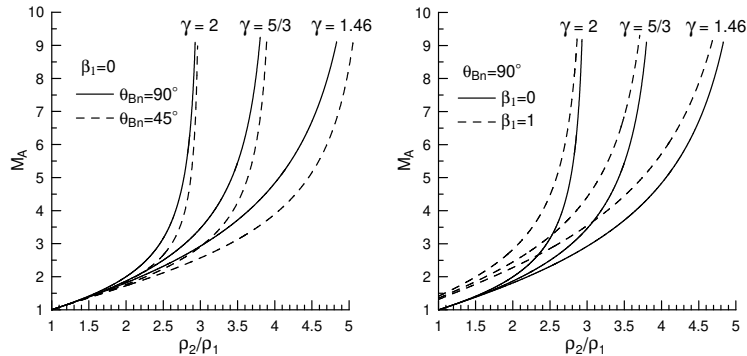


Figure 1. The ideal-MHD calculated dependences $M_A(\rho_2/\rho_1)$ in the flat shock front for various parameters of the upflow stream.

where the discontinuity moves to the parameter ratio at the discontinuity. Under the coronal conditions (at least, at $1-30R_\odot$ from the center of the Sun), the Alfvén velocity v_A far exceeds the sound velocity c_S . We can therefore take v_A for the typical velocity of disturbance propagation and find the dependence for the Alfvén Mach number $M_A = u/v_A$, where u is shock wave velocity. An expression for M_A at the flat shock discontinuity may be obtained in its analytical form (its derivation is presented in Appendix A).

It is so far impossible to measure magnetic field and temperature jumps at the shock discontinuity in the corona. But we can estimate the density ratio ρ_2/ρ_1 at the discontinuity from the white-light coronal brightness (index 1 means that the value corresponds to the undisturbed region ahead of the shock; 2 to the region behind it). Thus, our prime interest will be with the $M_A(\rho_2/\rho_1)$ dependence. The angle between the magnetic field direction ahead of the front and the normal to the wave front θ_{Bn} , adiabatic index γ , and the gas to magnetic pressure ratio β_1 still remain free parameters in the equation.

Figure 1 presents sets of $M_A(\rho_2/\rho_1)$ curves for $\gamma = 2, 5/3$ and 1.46 at different θ_{Bn} and β_1 . The left panel in Figure 1 shows the $M_A(\rho_2/\rho_1)$ dependences for $\beta_1 = 0$ and $\theta_{Bn} = 90^\circ$ and 45° (solid and dashed lines respectively). In the right panel Figure 1, $\theta_{Bn} = 90^\circ$ and $\beta_1 = 0$ and 1 . The dependences $M_A(\rho_2/\rho_1)$ at $\gamma = 5/3$ and $\beta_1 = 0$ coincide with similar dependences in Kantrowitz and Petschec, 1966 as presented in Kennel *et al.*, 1984. Figure 1 implies that the form of $M_A(\rho_2/\rho_1)$ for quasi-perpendicular shock waves ($\theta_{Bn} > 45^\circ$) depends little on θ_{Bn} and β_1 (at $0 \leq \beta_1 \leq 1$), but varies considerably depending on γ .

4. Analysis of experimental data

4.1. Event selection criteria

The main criterion for selecting events for the analysis was a reliable identification of shock fronts in the events. The identification was based on the following, previously obtained, results (Eselevich, 2010):

1. Ahead of CMEs with velocities exceeding $\approx 700 \text{ km s}^{-1}$, it is possible to record a shock wave and correctly measure its front width δ_F based on Mark 4 and LASCO C2 data. Our measurements have also shown that the shock front width δ_F is of order of the free proton path at $1.2R_\odot < R < 6R_\odot$, at least in a limited region located in the direction of the CME propagation. This provides evidence for the collisional mechanism of energy dissipation in the shock front at these distances.
2. A new discontinuity with width $\delta_F^* \ll \delta_F$ is observed to form at $R > 10R_\odot$ in the frontal part of the shock front. Within the experimental error, the value of $\delta_F^* \approx 0.1\text{-}0.2R_\odot$ is independent of R , being defined by the LASCO C3 spatial resolution. This brightness profile transformation from the front of width δ_F to the discontinuity of width $\delta_F^* \ll \delta_F$ was interpreted as transition from a collisional to a collisionless shock whose front width could not be resolved in coronal images.

The authors of Paper 1 registered brightness distribution discontinuities interpreted as shock waves, at the front of 13 selected CMEs moving at over 1500 km s^{-1} . Since the heliocentric distances at which the discontinuities were observed generally exceeded $6\text{-}10R_\odot$, and the minimum width of these discontinuities did not exceed $0.1\text{-}0.2R_\odot$, they appear to be associated with collisionless shock waves.

The flat shock wave condition $\delta_F^* \ll R_F$ (R_F is the radius of wavefront curvature) is better satisfied at large distances because it is there that fronts of width $0.1\text{-}0.2R_\odot$ are encountered. Moreover, the shock wave strength is sufficiently great ($\rho_2/\rho_1 \geq 2$) at these distances; i.e. the shock wave has already been formed and is stable. Therefore, we chose for our analysis those instances of time when the shock front was farther than $10R_\odot$.

Comparing the experimental data with the calculations of relations in the shock front requires absolute measurements of density; it is therefore very important to select events with minimised influence of factors affecting the measurements. We have chosen ten CMEs having shock waves in front, while keeping in mind the following requirements:

1. The origin of the CMEs was near the limb and they propagated in the plane of the sky; i.e., their measured positions and velocities were close to the true values.
2. 12-24 hours before each of the selected events, there were no other CMEs capable of noticeably changing the undisturbed solar wind conditions in the coronal region under study.

These events are listed in Table 1. The third column in the Table lists the coordinates of the CME-associated source region on the disk. The coordinates for the first two events were borrowed from Cremades and Bothmer, 2004, for the others from the catalogue Yashiro *et al.*, 2004. Since the origin of all the ten CMEs was near the limb, let us call them ‘limb CMEs’. According to the classification accepted in the catalogue Yashiro *et al.*, 2004, they include halo (events 3, 4, 7, 8 in Table 1) and partial halo CMEs (event 2). Let us not confuse limb CMEs with coronal ejections appearing at longitudes below $60\text{-}70^\circ$, which are therefore no limb CMEs.

Table 1.

1	2	3	4	5	6	7	8	9
Event	Time	Source coord.	R (R_{\odot})	δP (P_{MSB})	V (km s^{-1})	M_A	δN (cm^{-3})	ρ_2/ρ_1
1	1997 September 20							
	15:26:47	S24W102	23.3	2.5×10^{-13}	730	1.5	2.4×10^3	2.5
	16:01:23		25.4	1.7×10^{-13}	710	1.5	1.9×10^3	2.5
2	1998 April 20							
	11:48:11	S40W106	17.0	1.1×10^{-12}	1630	3.7	5.6×10^3	2.8
	12:38:07		24.0	3.5×10^{-13}	1640	4.7	3.6×10^3	3.4
3	1999 July 25							
	14:40:10	N23W81	11.0	2.4×10^{-12}	1280	2.1	5.1×10^3	1.6
	15:16:11		15.0	8.0×10^{-13}	1230	2.4	3.2×10^3	1.8
	16:16:17		21.0	3.2×10^{-13}	1070	2.5	2.5×10^3	2.2
	16:40:25		23.0	2.3×10^{-13}	970	2.3	2.2×10^3	2.3
4	2002 April 21							
	03:16:57	S16W84	26.1	2.9×10^{-13}	2422	7.9	3.5×10^3	3.7
5	2002 August 16							
	07:39:53	N07W83	13.5	1.7×10^{-12}	1340	2.5	5.5×10^3	2.1
	08:15:51		17.6	9.0×10^{-13}	1490	3.4	4.9×10^3	2.7
	08:39:50		21.0	3.7×10^{-13}	1390	3.5	2.9×10^3	2.4
	09:15:50		24.5	2.0×10^{-13}	1130	3.0	2.1×10^3	2.5
6	2003 November 4							
	13:41:57	N08W90	12.2	1.5×10^{-12}	1000	1.6	3.9×10^3	1.6
	14:17:55		15.4	6.0×10^{-13}	980	1.8	2.5×10^3	1.6
	14:41:47		17.3	7.7×10^{-13}	960	1.9	4.1×10^3	2.3
	15:17:27		20.3	4.0×10^{-13}	980	2.2	2.9×10^3	2.4
7	2005 August 23							
	15:40:45	S14W90	10.6	1.5×10^{-12}	1490	2.5	3.0×10^3	1.3
	16:16:53		15.1	3.5×10^{-13}	2070	4.5	1.4×10^3	1.3
	16:40:42		20.6	4.3×10^{-13}	2120	5.7	3.2×10^3	2.5
	17:16:50		25.4	1.8×10^{-13}	1550	4.6	2.1×10^3	2.5
8	2005 September 5							
	10:41:15	S07E81	12.2	8.0×10^{-13}	2070	3.9	2.1×10^3	1.3
	11:17:24		18.8	6.0×10^{-13}	2360	6.0	3.8×10^3	2.5
	11:41:16		24.1	3.5×10^{-13}	2590	8.1	3.6×10^3	3.4
9	2007 December 31							
	02:39:56	S08E81	11.4	1.1×10^{-12}	1150	1.9	2.5×10^3	1.3
	03:39:53		17.5	5.0×10^{-13}	1100	2.3	2.7×10^3	1.9
	04:40:06		22.7	2.7×10^{-13}	1000	2.4	2.5×10^3	2.4
10	2008 March 25							
	21:16:29	S13E78	15.2	6.5×10^{-13}	1040	2.0	2.7×10^3	1.7
	21:40:06		17.2	3.8×10^{-13}	990	2.0	2.0×10^3	1.6

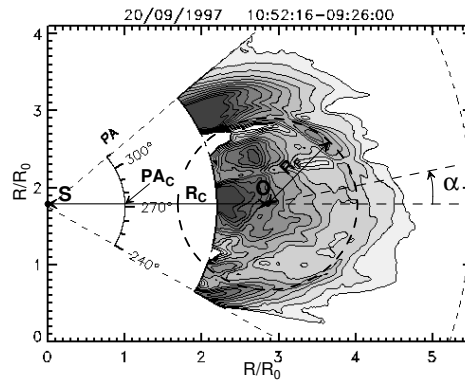


Figure 2. An example of a CME moving at a supersonic velocity (difference brightness isolines, LASCO C2 data). This figure includes the notations employed for referencing and constructing difference brightness profiles required for measurements in the shock front. The relevant explanations are given in the text.

4.2. Registering shock fronts ahead of CMEs

The shape of the CME outer boundary (and the adjacent shock wave) is usually nearly circular when the CME velocity exceeds the critical value u_C (Figure 2). The center of this circle (point O in the figure) may be defined by distance R_C from the center of the Sun (point S) and on the position angle PA_C . The difference brightness profiles $\Delta P(r)$ used to determine shock wave position were drawn from the center of the circle. The position of each profile was given by angle α to the direction of CME propagation. This angle is positive counterclockwise.

A shock associated discontinuity in difference brightness distributions is generally observed in a limited region in the direction of CME propagation (Eselevich, 2010). The value of α at which shocks were recorded did not exceed $\pm 10^\circ$ in all the ten selected events. For this range of angles α , the distances from the center of the Sun, R , and from the CME center, r , to the shock front may be related by a simple relation $R \approx R_C + r$, with an accuracy of $0.1R_\odot$. However, even a few-degree change in α and a few-pixel change in the CME center position significantly affect the discontinuity width as recorded in difference brightness profiles. An accurate choice of the O center position almost always provides the minimum discontinuity width comparable to the LASCO C3 spatial resolution.

Difference brightness profiles $\Delta P(r)$ drawn from the CME center were used to register shock fronts and measure their positions and amplitudes. Figures 3-6 present examples of such distributions for four events in Table 1. Each of the figures corresponds to one of the events, and each plot in the figures corresponds to a certain instant of time. The time difference used to construct the difference brightness, the CME center position (angle PA_C and distance R_C), and the direction along which the profile was drawn (angle α) are given for each plot. In all the cases, we used averaging in the range of angles $\delta\alpha = 2^\circ$. For convenience, each of the plots is reconstructed depending on the distance R from the center of the Sun, though the scanning direction may slightly differ from the radial direction. Each plot presents two distributions: 1) for the instants when CMEs

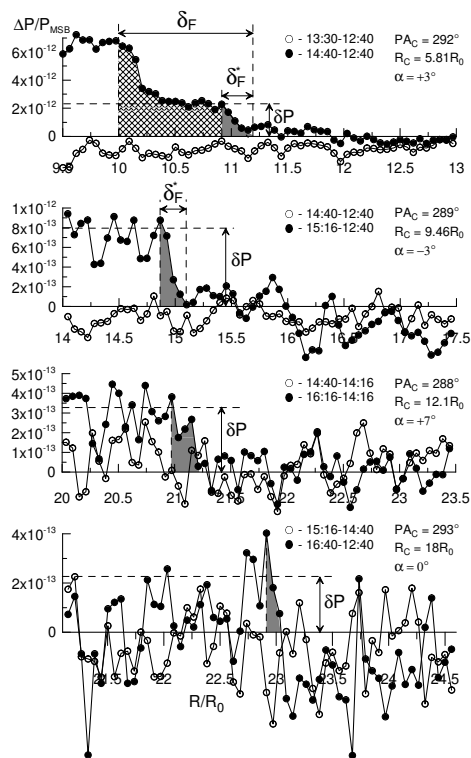


Figure 3. Black circles mark the difference brightness $\Delta P(R)$ distributions at successive instants of time for the 1999 July 25 CME. Light circles show the $\Delta P(R)$ distributions constructed for the instant of time just before the CME appears in the C3 field of view.

and shocks were recorded and 2) the difference brightness distributions for two neighboring instants before the CMEs appeared in the C3 field of view (the distributions are denoted by black and light circles respectively). The latter make it possible to estimate the noise level; in particular, they were used to find the error (1σ) in measuring the shock wave amplitude δP . At large distances, the noise level is comparable with the amplitude in some of the events.

All the events have common features, but differ in some respects. The differences require some commentary. The upper plots in Figures 3 and 4 show the stage when a collisional shock wave with front width δ_F transforms into a collisionless discontinuity with front width $\delta_F^* \ll \delta_F$, for the 1999 July 25 and 2007 December 31 events, respectively. Such a transformation usually takes place at $R < 10R_\odot$. The location and amplitude of δP were determined only for shock discontinuities with front width δ_F^* at $> 10R_\odot$. Another event occurred in the same coronal region approximately 12 hours before the CME, during the 1999 July 25 event (Figure 3). As a result, the undisturbed difference brightness constructed for a slightly earlier instant of time (light circles in the two upper plots) has a mean value that is significantly different from zero. In determining δP , we used averaging over a region behind the front whenever possible (Figures 3-6). The front width δ_F^* slightly varies but is almost constant at $> 10-15R_\odot$ (the

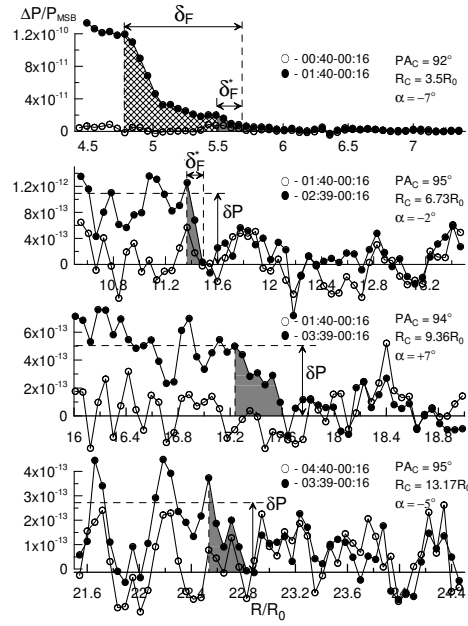


Figure 4. The same as in Fig. 3, but for the CME of 31 December 2007.

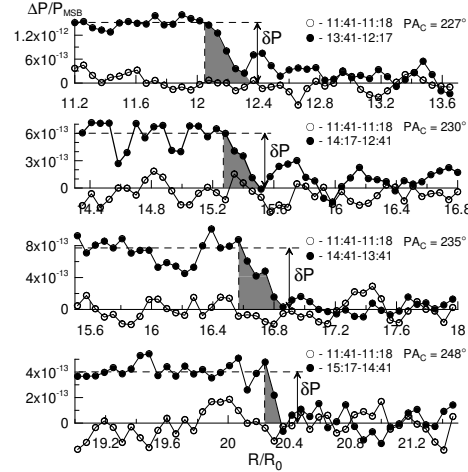


Figure 5. The same as in Fig. 3, but for the CME of 4 November 2003.

minimum value is $0.1-0.2R_\odot$), and the observed variations may have been due to noise.

The plots in Figures 3-6 as well as similar plots for other events were used to determine the shock wave distance from the center of the Sun (Column 4 in Table 1) and shock wave amplitude (Column 5) at a given instant of time. The obtained distances were employed to calculate shock wave velocities (Column 6). The velocity calculations took into account information on shock wave locations at $< 10R_\odot$ at earlier instants of time, not included in Table 1. The velocity at a

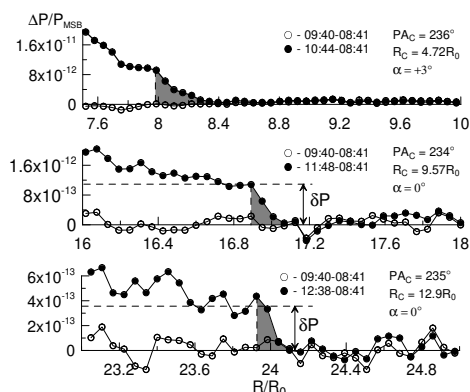


Figure 6. The same as in Fig. 3, but for the CME of 20 April 1998.

given instant of time is the average velocity for the intervals before and after this instant, except for the last instant, for which the velocity is simply the velocity as determined for the previous interval.

4.3. Estimating shock wave strength and comparing the results with MHD calculations

4.3.1. Experimental values for estimating the shock wave strength

Our aim is to compare the experimental dependence $M_A(\rho_2/\rho_1)$ with the analogous dependence derived from MHD calculations. The shock wave strength is defined as $\rho_2/\rho_1 \approx 1 + \delta N/N_0$, where δN is the absolute jump in electron density in the shock front, N_0 is the undisturbed plasma electron density immediately ahead of the shock front. To find M_A , we have to know the local Alfvén velocity (V_A) and the velocity (V_{SW}) of the solar wind relative to which the shock waves move.

Since N_0 , V_A and V_{SW} cannot be determined directly from the available experimental data, let us use their mean values typical of the quasi-stationary slow solar wind (SW) flowing in the streamer belt. The distance R dependences of V_{SW} , V_A , and N_0 (Figure 7) were taken respectively from (Wang *et al.*, 2000), (Mann *et al.*, 1999), and (Saito *et al.*, 1977). The validity of using the above dependences is obvious enough because the shock front parts under analysis are located near the axis of the CMEs propagating in the slow SW. This is also confirmed by the successful application of the dependences $V_{SW}(R)$ and $V_A(R)$ in the analysis in (Eselevich and Eselevich, 2008; see Figure 3) and, to some extent, of the dependence $N_0(R)$ in Paper 1. Applying $N_0(R)$, however, has a limitation mentioned above – there should be no other CMEs capable of changing the undisturbed SW conditions considerably in the region under study in the previous 24 hours. Column 7 in Table 1 gives calculated values of $M_A = (V - V_{SW})/V_A$, where V_{SW} and V_A values derived from the above experimental dependences.

The density jump δN in the shock front remains an unknown value and is to be determined. It is proportional to brightness jump δ in the difference

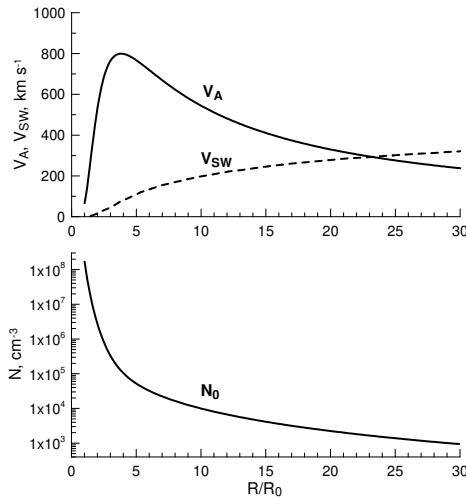


Figure 7. The experimental distributions employed to calculate M_A and ρ_2/ρ_1 . The upper panel: the solid curve is the Alfvén velocity $V_A(R)$ in Mann *et al.*, 1999, the dashed curve is the slow SW velocity $V_{SW}(R)$ in Wang *et al.*, 2000; the lower panel is the electron density in the corona in Saito *et al.*, 1977.

brightness distributions (Figures 2-6). The relationship between δ and δN depends on the unknown plasma distribution in the front. However, by specifying mean line-of-sight size l of the shock front, it is possible to calculate the mean density jump from the measured brightness discontinuity, using known relations (Billing, 1966). As long as we are dealing here with limb events, we may assume that the shock front is in the plane of the sky.

In Paper 1, the mean size of the shock front – $l = 1R_\odot$ – was used to calculate δN from δP for all the cases of the nonlimb CMEs. In what follows we will try to justify quantitatively a somewhat different value of l for the limb CMEs in Table 1, common for all the events under investigation as well.

4.3.2. Estimating the ultimate compression in a collisionless shock wave front

In the front of a quasi-perpendicular ($\theta_{Bn} > 45^\circ$) collisionless shock wave, heating of ions can occur in a plane perpendicular to the magnetic field direction (Zimbardo, 2009). This transverse motion is two-dimensional, which corresponds to two degrees of freedom ($i = 2$) and consequently to the adiabatic index $\gamma = (i + 2)/i = 2$. In the case of isotropic turbulence in the shock front, the number of degrees of freedom will tend to $i = 3$, and the adiabatic index to $\gamma = 5/3$ (Sagdeev, 1966). It is therefore reasonable to expect that the adiabatic index γ will be between $5/3$ and 2 in the front of a quasi-perpendicular collisionless shock. This means that maximum ρ_2/ρ_1 values at large Mach numbers must not exceed 4 (see Figure 1 or Appendix).

This assumption is supported by the results of direct measurements in the Earth’s bow shock and interplanetary shocks. These measurements do not produce $\rho_2/\rho_1 > 4$ even for the largest Mach numbers. To confirm this, the upper panel of Figure 8 presents the experimental dependences $M_A(\rho_2/\rho_1)$ for

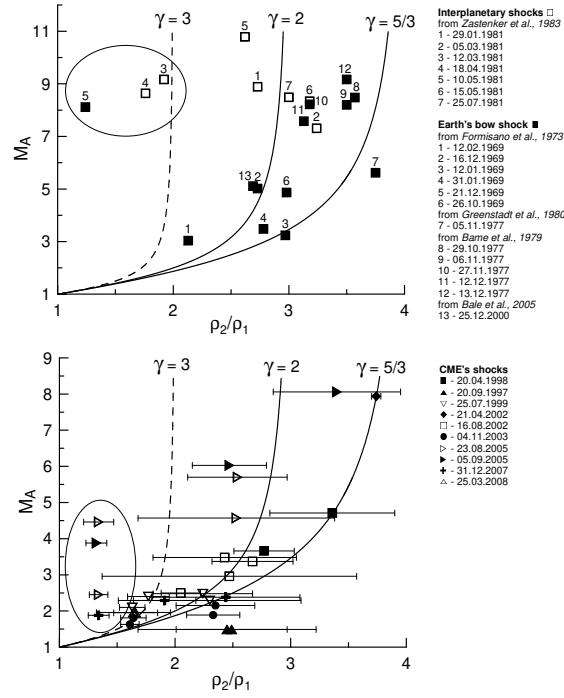


Figure 8. The experimental dependence $M_A(\rho_2/\rho_1)$: the upper panel is the bow shock (dark squares) and interplanetary shocks near the Earth's orbit (light squares); the lower panel displays ten shocks associated with limb CMEs. The solid and dashed curves denote ideal MHD calculations for perpendicular ($\theta_{Bn} = 90^\circ$) shocks at $\gamma = 5/3$, 2 and 3.

bow (solid marks) and interplanetary (light marks) shocks based on data of various authors. The values of ρ_2/ρ_1 in these dependences were taken from (Zastenker *et al.*, 1983) and (Formisano *et al.*, 1973; Greenstadt *et al.*, 1980; Bame *et al.*, 1979; Bale *et al.*, 2005) for interplanetary and bow shocks respectively. In some cases, the calculation of the Alfvén Mach number was based on hour-averaged OMNI data (<http://omniweb.gsfc.nasa.gov/>) on the magnetic field, SW density and velocity (for the bow shock). All the obtained ρ_2/ρ_1 do not exceed 4. This is also consistent with the $M_{MS}(\rho_2/\rho_1)$ plot in Figure 6 in Formisano *et al.*, 1973. That figure implies $\rho_2/\rho_1 \leq 4$ for all 42 crossings of the bow shock with large magnetosonic Mach numbers $M_{MS} = 4 - 12$ (by definition, $M_A \geq M_{MS}$).

The upper panel of Figure 8 implies that the experimental points are mainly located near the calculated curves for $\gamma = 5/3$ and $\gamma = 2$, i.e. in the collisionless shock front $\gamma \geq 5/3$. Note that the effective adiabatic index γ is smaller in the undisturbed SW. For example, Totten *et al.*, 1995 derived the empirical, mean adiabatic index for protons – $\gamma = 1.46 \pm 0.04 < 5/3$ – using Helios 1 data for the SW moving at $V_{SW} = 300 - 800 \text{ km s}^{-1}$. The fact that shocks are characterized by greater values of $\gamma \approx 5/3 - 2$ must be a result of collisionless processes inside the shock front.

Table 2.

α , deg.	R , R_\odot	δP , $\times 10^{-13} P_{MSB}$
-20	24.8	2.78
-17	26.0	2.86
-14	26.7	3.02
-11	26.9	2.00
-1	25.4	3.24
0	25.5	3.11
+3	26.4	2.57
+6	25.7	3.37
+10	26.8	2.94
+18	26.4	3.36
+19	26.3	2.65
26.1 ± 0.66		2.9 ± 0.4

4.3.3. Determining the effective line-of-sight size l of the shock front

By analogy with the heliosphere it is reasonable to expect that the adiabatic index $\gamma \geq 5/3$, and maximum density ratio is less than 4 for a collisionless shock in the solar corona. Let this conclusion serve as a basis for estimating l . For the purpose, we will examine the 2002 April 21 CME in more detail (number 4 in Table 1). This CME had the highest velocity of the ten selected events, and a maximum compression was observed in the shock front in front of the CME at about $26R_\odot$ from the center of the Sun at $t=03:16:57$. To enhance the accuracy, we constructed difference brightness distributions for several angles α in the range -20° to $+20^\circ$. Five of the distributions are shown in Figure 9. Besides, to determine the brightness jump δP the brightness profile was averaged on either side of the discontinuity. The event was accompanied by an intense flux of energetic particles which manifested themselves as bright dots and scratches on the coronal images. In some cases, filtration failed to completely remove such noise from the images. However, it can easily be detected in the brightness profiles (one of the examples is given in the upper plot of Figure 9). These parts of the brightness profiles were not used to determine δP .

Table 2 summarizes the measured δP values for various angles α and the distances at which they were observed. The distances differ slightly, indicating that the shock front is inhomogeneous along the direction of angle α . Determination of the front velocity and density discontinuity employed their mean values. The mean brightness discontinuity was $\delta P = 2.9 \times 10^{-13} P_{MSB}$, and the mean velocity $V = 2422 \text{ km s}^{-1}$. This velocity corresponded to $M_A = 7.94$ at the average distance $R = 26.1R_\odot$, where the shock front was recorded. The undisturbed density at the distance was $N_0 = 1.3 \times 10^3 \text{ cm}^{-3}$.

The brightness jump δP at a given distance R allows us to calculate δN and, taking N_0 into account, derive ρ_2/ρ_1 from it. As was stated above, we must set the shock front size l along the line of sight for the purpose. The curve

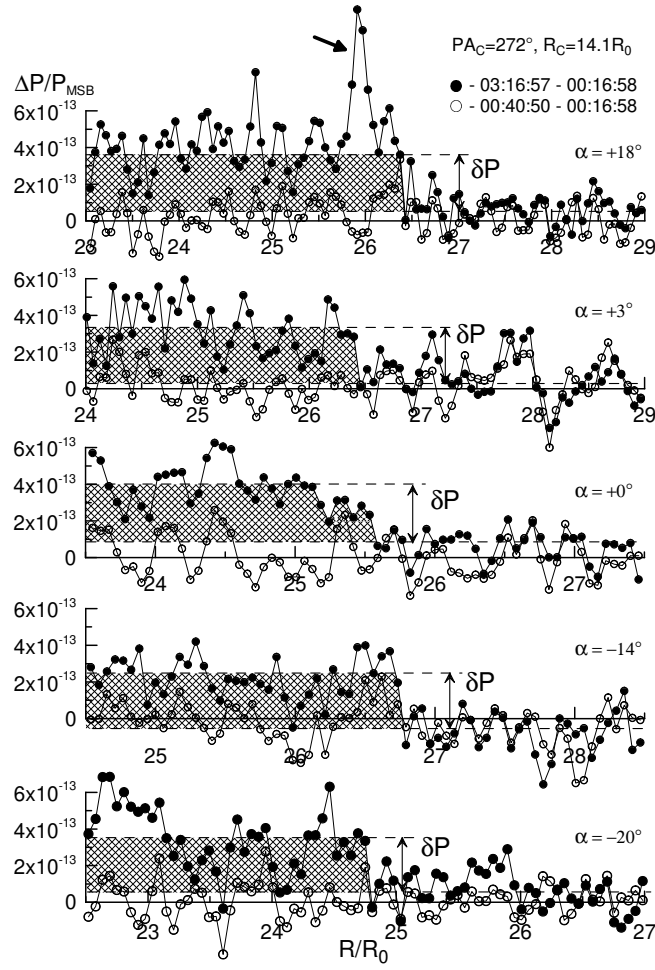


Figure 9. The difference brightness $\Delta P(R)$ distributions for several angles α for the CME of 21 April 2002; the shock front ahead of this CME had the highest compression of all the events under study.

in Figure 10 demonstrates how the calculated ρ_2/ρ_1 varies with the selected size l (in units of solar radius) under the conditions of the event under study ($\delta P = 2.9 \times 10^{-13} P_{MSB}$, $R = 26.1 R_\odot$, $N_0 = 1.3 \times 10^3 \text{ cm}^{-3}$). The main critical parameter is the adiabatic index γ because the β and θ_{Bn} dependences are rather weak. The range of maximum ρ_2/ρ_1 (i.e. as $M_A \rightarrow \infty$) for $\gamma = 5/3$ and 2 is indicated by hatching in Figure 10.

Let us assume that an extreme case is observed in the event: $\gamma = 5/3$, $\beta = 0$ and $\theta_{Bn} = 90^\circ$, i.e. there is a perpendicular shock with maximum compression. Then, the MHD calculations imply that the shock wave strength $\rho_2/\rho_1 = 3.74$, being close to the limiting value of 4. The plot in Figure 10 indicates that this strength corresponds to $l = 6.5 R_\odot$. This size was employed to calculate δN and

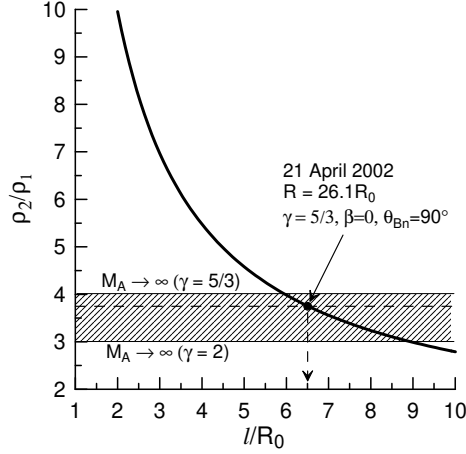


Figure 10. The ρ_2/ρ_1 values depending on the effective length l along the line of sight. They were calculated for the shock wave parameters at 03:16:57 ahead of the CME of 21 April 2002.

ρ_2/ρ_1 in all the ten selected events, their values are listed in columns 8 and 9 of Table 1.

4.3.4. Experimental dependence $M_A(\rho_2/\rho_1)$ for shocks in the corona

The calculated values in the lower panel of Figure 8 are used to compare the experimental dependence $M_A(\rho_2/\rho_1)$ for ten shocks with calculation results for perpendicular shocks ($\theta_{Bn} = 90^\circ$) at $\gamma = 5/3$ and $\gamma = 2$ (solid lines). The error bar due to the error in determining the brightness jump is indicated for the experimental points.

The dependences $M_A(\rho_2/\rho_1)$ suggest that as a whole they fit the calculated curves reasonably well in spite of the considerable scatter of experimental points. This allows the following conclusions to be made:

1. The choice of the mean value $l = 6.5R_\odot$ has proved to be reasonable enough despite the fact that the shock fronts in question were observed at various distances ($10R_\odot < R < 30R_\odot$) and had velocities $V \approx 800\text{-}2500 \text{ km s}^{-1}$.
2. The comparison results agree with the assumption that the effective adiabatic index γ , characterizing the processes within the front, is largely between 2 and 5/3, which corresponds to the effective number of degrees of freedom of motion being 2 to 3. This also testifies that the structures under investigation are collisionless shock fronts.

Of special notice are several outstanding points which correspond to shocks with sufficiently large Mach numbers but with small ρ_2/ρ_1 (outlined in upper and lower panels of Figure 8). They all lie to the left of the calculated curve with $\gamma = 3$. This corresponds to the effective number of degrees of freedom $\nu = 1$. If these points do not result from errors, we have to admit that in these cases the shock is not in a stationary state (physically justified dependence $M_A(\rho_2/\rho_1)$ becomes invalid for the points). It may result from various reasons. For example, in the

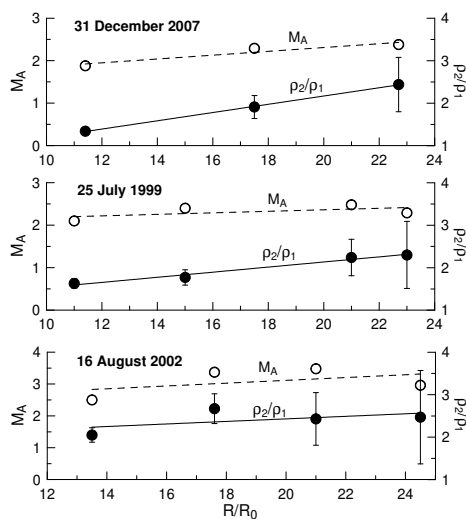


Figure 11. (M_A (light circles) and ρ_2/ρ_1 variations (dark circles) with distance in the events on 31 December 2007, 25 July 1999, and 16 August 2002.

case of the bow shock, the nonstationarity of the front may result from a change in the parameters of the upflow undisturbed SW.

The experimental results in Table 1 allow certain conclusions to be made with regard to how the shock front propagates in a coronal plasma where concentration rapidly decreases with distance. On the example of three different events in Figure 11, one can see that the shock wave strength and Alfvén Mach number, on the average, either change insignificantly or increase with distance at distances up to $R \leq 30R_\odot$. Such behaviour is also typical of other events.

5. Comparison with results of Paper 1

Density ratios ρ_2/ρ_1 (marked Γ_{CR}) have been found in Paper 1, for eleven shocks driven by CMEs moving at 1500-2000 km s⁻¹. The parameters of the events are in Tables 1 and 2 in Paper 1. They are numbered 1, 2, 4, 6, 7, 8, 9, 10, 11, 12, 14. The table velocity and distance values were used to calculate M_A values. The asterisks in Figure 12 mark the values corresponding to the events on the $M_A(\rho_2/\rho_1)$ plot. Since the ρ_2/ρ_1 values were derived in Paper 1 for $l = 1R_\odot$, the density ratios were recalculated for $l = 6.5R_\odot$ to compare them with our findings. The recalculated values are marked by dark circles in Figure 12. The light circles indicate our values (the same as in the lower panel of Figure 8).

It is obvious that there is a significant difference between findings in this paper and Paper 1: the density ratios in Paper 1 are much smaller than the values we obtain here. Note that the method for determining ρ_2/ρ_1 is identical in both papers. The only difference is the value of l : $1R_\odot$ in Paper 1 and $6.5R_\odot$ in our paper. There may be several reasons for the difference. We list them in the order of their influence on the result:

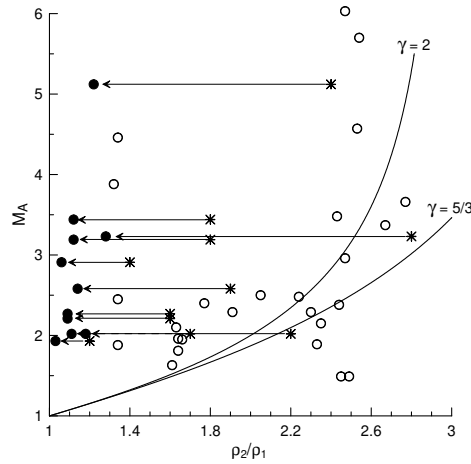


Figure 12. The experimental dependence $M_A(\rho_2/\rho_1)$ constructed from the ρ_2/ρ_1 values derived in this paper (light circles) and in Paper 1 for $l = 1R_\odot$ (asterisks) and recalculated for $l = 6.5R_\odot$ (dark circles).

1. presence of other CMEs capable of markedly changing the undisturbed solar wind density in the coronal region under study, less than twelve hours before the CME (events 1, 2, 4, 8, 10, 12 in Paper 1);
2. a non-stationary shock front, when the registration point is at $R < 10-15R_\odot$, and $\rho_2/\rho_1 < 2.0 - 2.5$ (events 1, 4, 6, 8, 9, 10, 11, 12, 14);
3. the CME source is rather far from the limb (nonlimb event) resulting in a noticeable error in determining distance R at which the shock is registered (and thus ρ_1 and V_A) and its velocity V . This may also result in decreased intensity of scattered light and, thus, decreased measured value of δ (events 1, 2, 6, 8, 9, 10, 11, 12).

Finally, the last comment. Paper 1 does not include $\rho_2/\rho_1 > 2.8$. But if we set $l = 1R_\odot$ for our events with $\rho_2/\rho_1 > 2.5$ at $l = 6.5R_\odot$, we will obtain $\rho_2/\rho_1 > 10$. Obviously, this value far exceeds the maximum values of the density ratios observed for collisionless shocks in the heliosphere (upper panel in Figure 9).

6. Conclusions

1. A brightness discontinuity, interpreted as a shock wave, was demonstrated to be registered in a limited region in front of each of the ten selected CMEs (propagating in the plane of the sky) along their travel directions. In various events, the shock wave velocity was $V \approx 800-2500 \text{ km s}^{-1}$.
2. Comparing the dependence of the Alfvén Mach number M_A on the shock wave strength ρ_2/ρ_1 , measured at $R > 10R_\odot$ from the center of the Sun, with ideal MHD calculations suggests that the effective adiabatic index γ , characterizing the processes inside the front is largely between 2 and 5/3. This corresponds to the effective number of degrees of freedom of motion 2 to 3. A similar dependence $M_A(\rho_2/\rho_1)$ was obtained for Earth's bow and

interplanetary collisionless shock waves. All these substantiate the assumption that the discontinuities in question in front of the CMEs at $R > 10R_\odot$ are collisionless shock waves.

Appendix

A. Deriving the dependence of the Alfvén Mach number on the density ratio at the flat shock using the ideal MHD approximation

A.1. Notations and initial equations

Let us consider a flat shock front. Index 1 will denote the undisturbed plasma region ahead of the front, index 2 the region behind the front. A front-associated coordinate system is used, i.e. the plasma velocity ahead of the front is the same as the front velocity. The front surface is in the yz plane, and the x axis is perpendicular to the surface. The coordinate system is chosen such that the magnetic field vectors and velocities lie in the xy plane. The magnetic field vector B_1 is at an angle, θ_{Bn} , to the x axis (i.e. to the normal to the front). Thus, the case of $\theta_{Bn} = 90^\circ$ corresponds to the perpendicular shock when the magnetic field vector is in the plane of the front.

According to Priest, 1982, the following conditions are satisfied at the shock discontinuity (in the CGS system):

$$\rho_2 v_{2x} = \rho_1 v_{1x} \quad (1)$$

$$p_2 + B_2^2/8\pi - B_{2x}^2/4\pi + \rho_2 v_{2x}^2 = p_1 + B_1^2/8\pi - B_{1x}^2/4\pi + \rho_1 v_{1x}^2 \quad (2)$$

$$\rho_2 v_{2x} v_{2y} - B_{2x} B_{2y}/4\pi = \rho_1 v_{1x} v_{1y} - B_{1x} B_{1y}/4\pi \quad (3)$$

$$(p_2 + B_2^2/8\pi)v_{2x} - B_{2x}(\mathbf{B}_2 \cdot \mathbf{v}_2)/4\pi + (\rho_2 e_2 + \rho_2 v_2^2/2 + B_2^2/8\pi)v_{2x} = (p_1 + B_1^2/8\pi)v_{1x} - B_{1x}(\mathbf{B}_1 \cdot \mathbf{v}_1)/4\pi + (\rho_1 e_1 + \rho_1 v_1^2/2 + B_1^2/8\pi)v_{1x} \quad (4)$$

$$B_{2x} = B_{1x} \quad (5)$$

$$v_{2x} B_{2y} - v_{2y} B_{2x} = v_{1x} B_{1y} - v_{1y} B_{1x} \quad (6)$$

here v is velocity, B is magnetic field, p is pressure, ρ is density, e is internal energy defined by $e = \frac{p}{(\gamma - 1)\rho}$ for the ideal polytropic gas, where γ is the adiabatic index.

Equation (1) is the mass conservation condition; equations (2) and (3) are the conservation conditions respectively of the x and y components of the momentum; equation (4) is the energy conservation condition. Equation (5) (following from $\text{div } \mathbf{B} = 0$) is the conservation condition of the normal component B_x of the magnetic field. Equation (6) is the continuity condition of the $[\mathbf{v} \times \mathbf{B}]$ value

following from the electric field tangential component continuity and magnetic field freezing-in condition.

Equations are written here in the general form, but the velocity and magnetic field z -components are zero throughout the selected coordinate system. At the shock discontinuity, the velocity changes – only the x component of velocity is present in region 1, whereas the y component is present in region 2 as well. The magnetic field, namely its y component, also varies in the front, whereas the x component remains unchanged.

A.2. Derivation and solution of main equations

Let us introduce the notation for the ratio of tangential (about a wave front) magnetic field components:

$$h = B_{2y}/B_{1y},$$

and the notation:

$$\Gamma = \gamma/(\gamma - 1).$$

We will additionally use the following expressions: $v_A = B/\sqrt{4\pi\rho}$ for the Alfvén velocity, $M_A = v_{1x}/v_{A1}$ for the Alfvén Mach number, and $\beta = \frac{p}{B^2/8\pi}$ for the gas to magnetic pressure ratio.

Equation (3), with due account for (1) and (5), may be used to express the tangential velocity component appearing behind the front:

$$v_{2y} = \frac{B_1}{4\pi\rho_1 v_{1x}} (h - 1) \cos^2 \theta_{Bn} \tan \theta_{Bn}$$

Substituting the v_{2y} expression into (6) and taking (1) into account, we get:

$$\frac{v_{2x}}{v_{1x}} = \frac{\rho_1}{\rho_2} = \frac{1}{h} \left(1 + \frac{h-1}{M_A^2} \cos^2 \theta_{Bn} \right) \quad (7)$$

The expression (7) relates the density ratio ρ_2/ρ_1 and the Alfvén Mach number M_A . However, this expression also includes the ratio between magnetic field tangential components, h ; thus we must construct and solve an equation system to express M_A in terms of h .

Dividing both sides of Equation (2) by $\rho_1 v_{1x}^2$ with due account for (5) and expression for v_{2x}/v_{1x} yields:

$$\frac{1}{h} \left(1 + \frac{h-1}{M_A^2} \cos^2 \theta_{Bn} \right) (1 + \alpha_2) = \frac{\beta_1}{2M_A^2} + \frac{(1-h^2) \sin^2 \theta_{Bn}}{2M_A^2} + 1 \quad (8)$$

We introduce the notation $\alpha_2 = \frac{p_2}{\rho_2 v_{2x}^2}$ here.

Dividing both sides of Equation (4) by $\frac{\rho_1 v_{1x}^3}{2}$ and substituting expressions for v_{2y} and v_{2x}/v_{1x} , we obtain a second equation:

$$(1 + 2\Gamma\alpha_2) \frac{1}{h^2} \left(1 + \frac{h-1}{M_A^2} \cos^2 \theta_{Bn}\right)^2 + \frac{2(h-1) \sin^2 \theta_{Bn}}{M_A^2} + \frac{(h-1)^2 \sin^2 2\theta_{Bn}}{4M_A^4} = \frac{\Gamma\beta_1}{M_A^2} + 1 \quad (9)$$

Thus there are two equations to express M_A in terms of h . Expressing α_2 from the first equation and substituting it into the second one produces, after some simplification:

$$\frac{h-1}{hM_A^2} \left((M_A^2 - \cos^2 \theta_{Bn})(M_A^2(1+h-2\Gamma) + h\beta_1\Gamma - (h-1)(2\Gamma-1)\cos^2 \theta_{Bn}) + h \sin^2 \theta_{Bn} (M_A^2(h(\Gamma-2) + \Gamma) + (h-1)(h(\Gamma-1) + \Gamma)\cos^2 \theta_{Bn}) \right) = 0 \quad (10)$$

This equation has two solutions for M_A^2 :

$$M_A^2 = \frac{1}{2(1+h-2\Gamma)} \left(-h\beta_1\Gamma + 2(1+(h-2)\Gamma)\cos^2 \theta_{Bn} - \frac{h(h(\Gamma-2) + \Gamma)\sin^2 \theta_{Bn}}{\pm \sqrt{h^2(4(\Gamma-1)^2\cos^4 \theta_{Bn} + (\beta_1\Gamma + (h(\Gamma-2) + \Gamma)\sin^2 \theta_{Bn})^2 - 4(\Gamma-1)\cos^2 \theta_{Bn}(\beta_1\Gamma + (1+h^2 - (1+h)\Gamma)\sin^2 \theta_{Bn})}} \right) \quad (11)$$

The solution with ‘+’ before the root gives the trivial value $M_A^2 = 0$ at $\theta_{Bn} = 90^\circ$ and physically infeasible values $M_A^2 < 0$ at $\theta_{Bn} \neq 90^\circ$. Of interest is therefore the second solution with ‘-’ before the root.

A.3. Extreme cases

Let us consider some extreme cases of the solution. We may set $\beta_1 = 0$ for plasma totally controlled by the magnetic field, and $\gamma = 5/3$ and correspondingly $\Gamma = 2.5$ for gas with three degrees of freedom.

In the perpendicular shock case ($\theta_{Bn} = 90^\circ$), the expression for M_A^2 is simplified and takes the form:

$$M_A^2 = \frac{h(2.5 + 0.5h)}{4 - h}$$

If $M_A^2 = 1$, then $h = 1$, and if $M_A^2 \rightarrow \infty$, then $h \rightarrow 4$. As is evident from (8), the density ratio in the shock front in this case simply equals the magnetic field tangential component ratio, i.e. $\rho_2/\rho_1 = h$.

In the parallel shock case ($\theta_{Bn} = 0^\circ$), $M_A^2 = 1$ for any h because it is an extreme case of shock wave unaffected by the magnetic field.

In the general case of $\beta_1 \neq 0$, $M_A^2 > 1$ for $h = 1$ because the characteristic velocity of disturbance propagation in the plasma will be the fast magnetosonic wave velocity rather than the Alfvén velocity v_A (Priest, 1982)

$$v_{MS} = \sqrt{\frac{1}{2}(c_s^2 + v_A^2) + \frac{1}{2}\sqrt{c_s^4 + v_A^4 - 2c_s^2v_A^2 \cos 2\theta_{Bn}}}$$

where c_s is the sound velocity. In this case it is more correctly to try to find the dependence of the magnetosonic Mach number $M_{MS} = v/v_{MS}$ on density and magnetic field ratios.

Acknowledgements The work was supported by the Program No. 16 part 3 of the Presidium of the Russian Academy of Sciences, Program of State Support for Leading Scientific Schools NS-2258.2008.2, and the Russian Foundation for Basic Research (Project No. 09-02-00165a). The SOHO/LASCO data used here are produced by a consortium of the Naval Research Laboratory (USA), Max-Planck-Institut fuer Aeronomie (Germany), Laboratoire d'Astronomie (France), and the University of Birmingham (UK). SOHO is a project of international cooperation between ESA and NASA.

References

- Bale, S.D., Balihin, M.A., Horbury, T.S. *et al.*: 2005, Quasi-perpendicular shock structure and processes. *Space Sci. Rev.* **118**, 161-203. DOI: 10.1007/s 11214-005-3827-0.
- Bame, S.J., Asbridge, J.R., Gosling, J.T., Halbig, M., Paschmann, G., Scopke, N., Rosenbauer, H.: 1979, High temporal resolution observations of electron heating at the bow shock. *Space Sci. Rev.* **23**, 75-92.
- Billing, D.E.: 1966, *A guide to the solar corona*, Academic press, New York, 150.
- Brueckner, G.E., *et al.*: 1995, The Large Angle Spectroscopic Coronagraph (LASCO). *Solar Phys.* **162**, 357-402.
- Cremades, H., Bothmer, V.:2004, On the three-dimensional configuration of coronal mass ejections. *Astron. Astrophys.* **422**, 307-322. DOI: 10.1051/0004-6361:20035776
- Eselevich, M.V., Eselevich, V.G.: 2007, First experimental studies a perturbed zone preceding the front of a coronal mass ejection. *Astronomy Reports* **51**, 947-954.
- Eselevich, M.V., Eselevich, V.G.: 2008, On formation of a shock wave in front of a coronal mass ejection with velocity exceeding the critical one. *Geophys. Res. Lett.* **35**, L22105, doi:10.1029/2008GL035482.
- Eselevich, M.V.: 2010, Detecting the widths of shock fronts preceding coronal mass ejections. *Astronomy Reports* **54**, 173-183.
- Formisano, V., Hedgecoc, P.C., Moreno, G., Palmiotto, F., Chao, J.K.: 1973, Solar wind interaction with the Earth's magnetic feild. 2. Magnetohydrodynamic Bow Shock. *J. Geophys. Res.* **78**, 3731-3744.
- Greenstadt, E.W., Russel, C.T., Gosling, J.T., Bame, S.J., Paschmann, G., Park, G.K., Anderson, K.A., Scarf, F.L., Anderson, K.A., Gurnett, D.A., Lin, R.P., Lin, C.S., Reme, H.: 1980, A macroscopic profile of the typical quasi-perpendicular bow shock: Isee 1 and 2. *J. Geophys. Res.* **85**, A5, 2124-2130.
- Kantrowitz, A.R., Petschec, H.E.: 1966, MHD characteristics and shock waves. In: Kunkel, W.B. (ed.) *Plasma Physics in Theory and Application*, McGraw-Hill, New York.
- Kennel, C.F., Edmiston, J.P., Hada, T.: 1984, A quarter century of collisionless shock research. Based upon the opening lecture presented by C. F. Kennel at the A.G.U. Chapman Conference on Collisionless Shock in the Heliosphere, Napa Valley, California, February 20. 1984 Center plasma physics and fusion engineering, University of California Los Angeles.

- Manchester IV, W.B., Vourlidas, A. Tóth, G., Lugaz, N. Roussev, I.I., Sokolov, I.V., Gombosi, T.I., De Zeeuw, D.L., Opher, M.: 2008, Three-dimensional MHD simulation of the 2003 October 28 coronal mass ejection: comparison with LASCO coronagraph observations. *Astrophys. J.* **648**, 1448-1460.
- Mann, G., Aurass, H., Klassen, A., Estel, C., Thompson, B.J.: 1999, Coronal Transient Waves and Coronal Shock Waves. In: Vial, J.-C., Kaldeich-Schümann, B. (eds.) *proc. 8th SOHO Workshop Plasma Dynamics and Diagnostics in the Solar Transition Region and Corona*, Paris, France, 22-25 June 1999, 477-481.
- Ontiveros, V., Vourlidas, A.: 2009, Quantitative measurements of coronal mass ejection-driven shocks from LASCO observations. *Astrophys. J.* **693**, 267-275.
- Priest, E.R.: 1982, in Reidel, D. (ed), *Solar Magnetohydrodynamics*. Dordrecht, Holland.
- Saito, K., Poland, A.I., Munro, R.H.: 1977, A study of the background corona near solar minimum. *Solar Phys.* **55**, 121-134.
- Sagdeev, R.Z.: 1966, Cooperative phenomena and shock waves in collisionless plasma. In: Leontovich, M.A. (ed) *Reviews of Plasma Physics*, **4**, Consultants Bureau, N.Y.
- Totten, T.L., Freeman, J.W., Arya, S.: 1995, An empirical determination of the polytropic index for the free-streaming solar wind using HELIOS 1 data. *J. Geophys. Res.* **100**, 13-17.
- Vourlidas, A., Wu, S.T., Wang, A.H., Subramanian, P., Howard, R.A.: 2003, Direct detection of a coronal mass ejection-associated shock in Large Angle and Spectrometric Coronagraph experiment white-light images. *Astrophys. J.* **598**, 1392-1402.
- Wang, Y.-M., Sheeley, N.R., Socker, D.G., Howard, R.A., Rich, N.B.: 2000, The dynamical nature of coronal streamers. *J. Geophys. Res.* **105**, 25133-25142.
- Yashiro, S. Gopalswamy, N. Michalek, G., St. Cyr, O.C. Plunkett, S.P. Rich, N.B. Howard, R.A.: 2004, A catalog of white light coronal mass ejections observed by the SOHO spacecraft. *J. Geophys. Res.* **109**, A07105. doi:10.1029/2003JA010282.
- Zastenker, G.N., Borodkova, N.L., Vaisberg, O.L., Omel'chenko, A.N., Yermolaev, Yu.I., Balebanov, V.M.: 1983, Interplanetary shock waves in the period after the solar maximum year: observation Prognoz-8 satellite. Preprint 841, Space Research Institute, Moscow.
- Zimbardo, G.: 2009, More than mass proportional heating of heavy ions by collisionless quasiperpendicular shocks in solar corona. Conference Solar Wind 12, Saint-Malo, France, 21-26 June 2009. arXiv:0906.3243.